Sensitivity study of resolution and convergence requirements for the extended overlap region in wall-bounded turbulence

Sergio Hoyas [*]
Instituto Universitario de Matemática Pura y Aplicada,
Universitat Politècnica de València, Valencia 46022, Spain

Ricardo Vinuesa [†]
FLOW, Engineering Mechanics, KTH Royal Institute of Technology, Stockholm 100 44, Sweden

Peter Schmid [‡]
Department of Mechanical Engineering, Division of Physical Sciences and Engineering (PSE),
King Abdullah University of Science and Technology (KAUST), Thuwal 23955-6900, Saudi Arabia

Hassan Nagib [§]
Mechanical, Materials and Aerospace Engineering, Armour College of Engineering,
ILLINOIS TECH, Chicago, Illinois 60616, USA

Direct numerical simulations (DNSs) are among the most powerful tools for studying turbulent flows. Even though the achievable Reynolds numbers are lower than those obtained through experimental means, DNS offers a clear advantage: The entire velocity field is known, allowing for the evaluation of any desired quantity. This capability includes the computation of derivatives of all relevant terms. One such derivative provides the indicator function, which is the product of the wall distance and the wall-normal derivative of the mean streamwise velocity. This derivative may depend on mesh spacing and distribution, but it is extremely affected by the convergence of the simulation. The indicator function is crucial for understanding inner and outer interactions in wall-bounded flows and describing the overlap region between them. We find a clear dependence of this indicator function on the mesh distributions we examine, raising questions about classical mesh and convergence requirements for DNS and achievable accuracy. Within the framework of the logarithmic plus linear overlap region, coupled with a parametric study of channel flows and some pipe

*Contact author: serhocal@mot.upv.es
†Contact author: rvinuesa@mech.kth.se
‡Contact author: peter.schmid@kaust.edu.sa
§Contact author: nagib@iit.edu

flows, sensitivities of extracted overlap parameters are examined. This study reveals a path to establishing their high-Re_τ or nearly asymptotic values at modest Reynolds numbers, but larger than the ones used in this work, accessible by high-quality DNS with reasonable cost.

Over the past half century, direct numerical simulation (DNS) has become a widely used approach to study fundamental aspects of wall-bounded turbulence [1–5]. One topic within wall-bounded turbulence that has received extensive attention from the research community due to its significant implications is the overlap region of the mean velocity profile. In this overlap region, the large structures that populate the outer layer coexist with the smaller ones, which are strongly influenced by the wall and viscous effects. According to the classical literature, the mean velocity profile in this overlap region follows the well-known logarithmic law, with its Kármán constant κ [6]:

$$\overline{U_{x_{\mathrm{in}}}}^+(y^+ \gg 1) = \frac{1}{\kappa} \ln y^+ + B_0. \tag{1}$$

In this equation, $\overline{U_x}$ is the streamwise mean velocity, i.e., we decompose the instantaneous velocity as $U_x = \overline{U_x} + u$. The subindex "in" (for inner) indicates that we are using the wall characterization of this velocity. Over the years, this has been a topic of active study, and the universality of the logarithmic law and the von Kármán coefficient has been occasionally challenged or reaffirmed (see, e.g., Refs. [7–10]). Recently, Monkewitz and Nagib (MN) [11] shed additional light on this topic, extending the accumulated knowledge during the past century. Monkewitz and Nagib's main point is to consider in the inner asymptotic expansion a term proportional to the wall-normal coordinate, $O(\mathrm{Re}_\tau^{-1})$, which is of the same order as the logarithmic term, and different from other previous works [12,13], where it is a higher-order term. Here $\mathrm{Re}_\tau = u_\tau \delta / \nu$ is the friction Reynolds number, with δ a characteristic outer length. This δ can be considered as the radius R in pipes and the semiheight h in channels or δ_{99} in boundary layers. Following MN, the pure logarithmic law is not observed in channels, pipes, and other flows with streamwise pressure gradients [14] for all Re_τ. Monkewitz and Nagib's extended matched asymptotics method reveals an additional term in the expansion of the velocity for this layer, leading to an extra contribution in the overlap layer in the form $S_0 y^+ \mathrm{Re}_\tau^{-1}$, where S_0 is a coefficient.

Interestingly, the overlap region represented by combined logarithmic and linear terms exhibits values of the von Kármán coefficient κ consistent with those obtained from skin-friction relations, a fact that suggests that this approach can reveal high-Re trends even at moderate Reynolds numbers (see, for example, [14,15]). The main point of this matched asymptotic theory is to use a new expression in the overlap region for $\overline{U}_x$. Monkewitz and Nagib's formula reads

$$\overline{U_{x_{\mathrm{in}}}}^+(y^+ \gg 1) \sim \kappa^{-1} \ln y^+ + B_0 + B_1/\mathrm{Re}_\tau + S_0 y^+/\mathrm{Re}_\tau. \tag{2}$$

To obtain accurate values of these coefficients, it is necessary to address two fundamental issues: To find κ, the challenge is to identify the location and extent of the overlap region, which is weakly dependent on the Reynolds number [11], and to obtain the correct value of S_0, it is necessary to obtain with high accuracy the values of $\mathrm{d}\overline{U_x}^+/\mathrm{d}y^+$. For the latter, it is possible to obtain an equation for the values of κ and S_0 through the indicator function

$$\Xi(y^+) = y^+ \frac{\mathrm{d}\overline{U_x}^+}{\mathrm{d}y^+}. \tag{3}$$

TABLE I. DNS case labels and nomenclature of pipe P and channel C flows, with NR and HR representing classical and high resolution in y and C and F denoting coarse and fine in x and z. Here L_x and L_z are periodic streamwise and spanwise dimensions; δ is either the channel half height or pipe radius; Δx^+ and Δz^+ are inner-scaled resolutions in terms of dealiased Fourier modes; the wall-normal direction is indicated in both flows by y; N_x, N_z, and N_y are the numbers of collocation points in three different directions; the time span of the simulation is given in terms of eddy turnovers $u_\tau T/\delta$; and ε is a measure of convergence, defined in [17]. The last two columns give the values of κ and S_0 as defined in Eq. (4). Colors in the first column are used in Figs. 1(a), 3, and 4, with dashed lines for the channel.

Case	Re$_\tau$	L_x/δ	L_z/δ	Δx^+	$\Delta(R\theta^+)$	max(Δy^+)	min(Δy^+)	N_x	N_z	N_y	ETT	$\varepsilon \times 10^{-4}$	κ	S_0
PNRF	549	10π	2π	5.62	3	3.2	0.018	3072	1152	256	93	1.2	0.444	2.69
PHRF	549	10π	2π	5.62	3	1.6	0.005	3072	1152	512	87	2.6	0.449	2.88
PNRC	549	10π	2π	11.2	4.5	3.2	0.018	1536	768	256	184	0.8	0.451	2.77
PHRC	549	10π	2π	11.2	4.5	1.6	0.005	1536	768	512	56	3.8	0.429	2.53
CNRC	546	8π	3π	9	4.5	5.85	0.8	1536	1152	251	150	0.7	0.434	1.61
CHRC	546	8π	3π	9	4.5	1.68	0.05	1536	1152	901	150	0.3	0.438	1.68

From Eqs. (2) and (3), one can obtain the equation for κ and S_0:

$$\Xi(y^+) = \kappa^{-1} + S_0 y^+/\mathrm{Re}_\tau = \kappa^{-1} + S_0(y/\delta). \tag{4}$$

Thus, to accurately determine S_0, it is necessary to compute the indicator function with high accuracy, an aspect that has not been sufficiently investigated in the literature. Early concerns about classical resolution practices appeared in DNS of homogeneous isotropic turbulence [16]. While a convergence criterion exists for fully developed flows [17] and the domain size of the problem has been examined in depth [18,19], the necessary grid spacing has received much less attention. Examples can be found in some very large simulations [4,20], where the authors only report their mesh size and compare their results with those in previous references, which basically do the same.

We have performed two different numerical experiments to examine this issue and its implications. The details can be found in Tables I and II. On the one hand, we have studied a smooth pipe of radius R and length $L_x = 10\pi R$ for $\mathrm{Re}_\tau = 550$. We will also use y to indicate the distance to the

TABLE II. Channel-flow DNS cases for higher Re$_\tau$ than in Table I, with the nomenclature Hx, Nx, and Dx representing half, classical, and double resolution in x and using the same convention for z. Other notation is described in Table I. A theoretical cost of each simulation compared to the case with the classical resolution, C83NxNz, is estimated in the last column for one ETT. Colors given in third column are used in Figs. 1(b) and 5.

	Case	Re$_\tau$	Line	L_x/δ	L_z/δ	Δ_x^+	Δ_z^+	max(Δy^+)	min(Δy^+)	N_x	N_y	N_z	ETT	$\varepsilon \times 10^{-4}$	κ	S_0	Cost
C21NxNz	1000	…..	2π	π	8.2	4.1	7.3	0.4	768	383	768	160	2.4	0.386	1.27	0.08
C42NxNz	1000	_ _ _	4π	2π	8.2	4.1	7.3	0.4	1536	383	1536	50	3.1	0.415	1.77	0.33
C83NxNz	1002	▬▬	8π	3π	8.2	4.1	7.3	0.4	3072	383	2304	47	1.5	0.399	1.36	1
C163NxNz	1001	_ _ _	16π	3π	8.2	4.1	7.3	0.4	6044	383	2304	44	0.9	0.401	1.46	2
C83DxDz	1000	▬▬	8π	3π	4.1	2.0	7.3	0.4	6044	383	4608	29	2.8	0.400	1.52	8
C83NxDz	1000	_ _ _	8π	3π	8.2	2.0	7.3	0.4	3072	383	4608	36	2.0	0.392	1.39	2
C83DxNz	1002	…..	8π	3π	4.1	4.1	7.3	0.4	6044	383	2304	15	3.3	0.396	1.27	4
C83HxHz	1017	_ _ _	8π	3π	16.4	8.2	7.3	0.4	1536	383	1152	83	0.2	0.415	1.60	0.12
C83HxNz	1001	▬▬	8π	3π	16.4	4.1	7.3	0.4	1536	383	2304	37	0.8	0.409	1.57	0.25
C83NxHz	1018	…..	8π	3π	8.2	8.2	7.3	0.4	3072	383	1152	10	10	0.394	1.29	0.5
CL83NxNz	1000	…..	8π	3π	8.2	4.1	2.5	0.08	3072	1085	2304	25	9.4	0.394	1.42	3
C86NxNz	1001	_._..	8π	6π	8.2	4.1	7.3	0.4	3072	383	2304	35	3.4	0.401	1.44	2
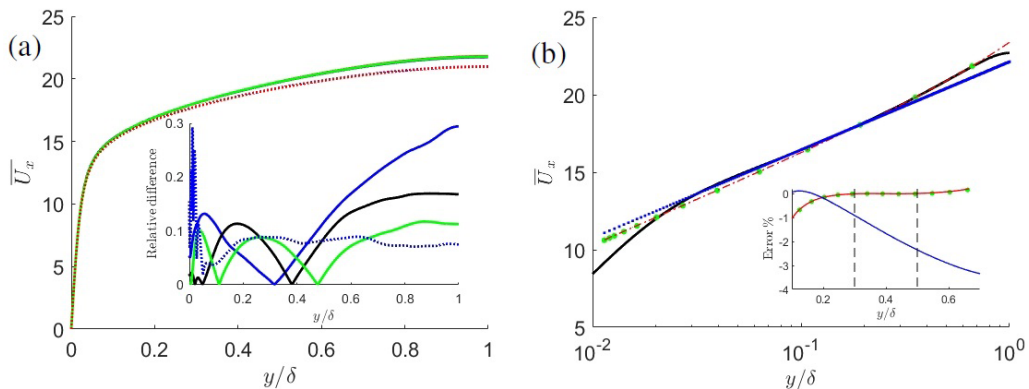
FIG. 1. (a) Profile of $\overline{U_x}$ for the pipe and channel cases of Table I, with the inset showing the difference between the finest resolution case and others. (b) Plot of $\overline{U_x}$ (black line) for case CL83NxNz of Table II, with overlap relations given by the classic logarithmic law (1) (blue dotted line) and the logarithmic line, Eq. (2) (red dash-dotted line) and Eq. (4) (green dots). The inset depicts the percent error for each.

wall on the pipe to facilitate the notation. We have used four different meshes, as seen in Table I. The base mesh is the case PLRC with a classical channel resolution in x and $R\Theta$. On the other hand, the mesh in the radial direction has twice the number of points needed in a channel due to the skewness of the cells near the pipe center. Using this large number of points, the wall-normal grid spacing for the pipes is below the Kolmogorov scale throughout the computational domain. Starting with the PLRC case, we doubled the cells in the radial direction (PHRC), the azimuthal streamwise one (PLRF), and all of them (PHRF). All these simulations ran for at least 55 eddy-turnover times (ETTs), defined as Tu_τ/R.

On the other hand, we have run two sets of channel-flow simulations. The first one (CLRC and CHRC) is a simulation with the same mesh in x and z as in the work of Hoyas and Jiménez [1] but different for y, as the second one uses a mesh considered enough for $Re_\tau = 3000$ [21]. The second data set (Table II) covers many different simulations for $Re_\tau = 1000$, varying the mesh and the channel geometry.

Two different codes were employed. OPENPIPEFLOW was used to run the pipe simulations [20]. The code LISO was used for running the channel flow [1,22,23]. Both codes employ Fourier-decomposition techniques in the streamwise and spanwise or azimuthal directions. OPENPIPEFLOW uses a seventh-order finite-difference scheme in the wall-normal direction, while LISO uses a tenth-order compact-finite-difference scheme [22].

In the case of the pipe flow, the difference among the four simulations appears small when analyzing the streamwise mean velocity, as displayed in Fig. 1(a). Comparable differences are found for the cases in Table II. Notice that the differences among the different cases are below 0.2% across the whole domain. A second very important point is the interval of validity of the logarithmic and log-lin layers. In Fig. 1(b) $\overline{U_x}$ is plotted for the "standard" case CL83NxNz [24]. As expected, there are only a few points in the logarithmic region, but the log-lin interval is considerably larger. Notice that the curves obtained using Eq. (2) (red dash-dotted curve) or Eq. (4) (green dots) collapse completely. The possible error in computing κ, S_0, and any other coefficient is then independent of the quality of the derivative.

For a detailed examination of the effects of the DNS resolution in the wall-normal direction and to select the best overlap limits to examine all channel cases, we compare two cases in Fig. 2, with one of them using the classical resolutions and the other with the resolution in wall-normal direction doubled. Here we plot the L^2-norm of the difference between the function and the model. As we can see, a larger mesh implies a more ordered distribution of isolines of the error. This is directly related to a better convergence. A second point is that the error is quite flat around the interval of
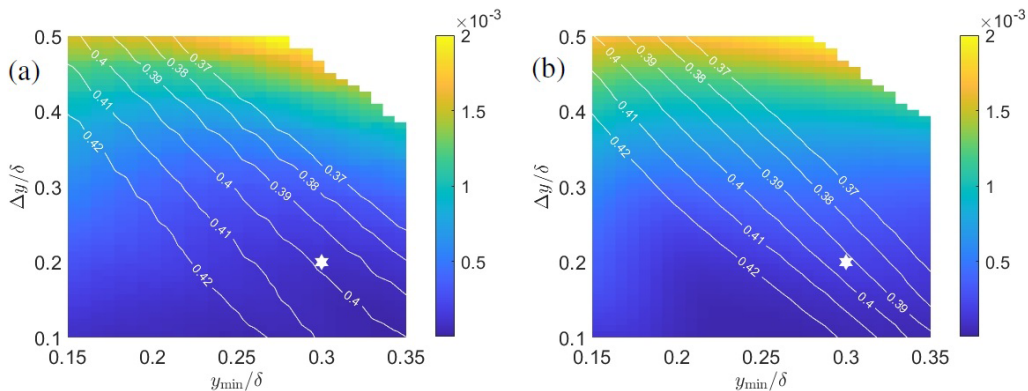
FIG. 2. Plot of the L^2-norm of error between the log-lin overlap (4) and DNS data for different intervals for (a) case C83NxNz and (b) case CL83NxNz. The horizontal axis represents the starting point of the overlap region and the vertical axis is the width of the overlap region. White lines are contours of constant κ. White stars indicate selected overlap limits for all other figures.

interest $0.3 < y/\delta < 0.5$. We will use this interval from now on, also given that for larger Reynolds numbers, there seems to be a collapse of Ξ on it [15].

Part of the motivation to use the indicator function Ξ is to allow extracting the overlap parameters from experimental data where the accuracy of the measurements is not sufficient and the density and regular spacing of the data are not adequate for obtaining profile derivatives. As we already said, we achieve identical results from the mean velocity profile or its indicator function after differentiation. Even such accuracy is not sufficient to utilize the indicator function Ξ to extract reliable coefficients of overlap regions. As shown in Fig. 3(a), the different curves of Ξ for the Table I cases do not collapse exactly in the region of interest, where the slope value of Ξ is critical. This is more clearly appreciated in Fig. 3(b), where the differences across cases can be more clearly assessed. Notice that the finer mesh, the PHRF case, corresponds to the red solid line. The other three cases have not converged to the PHRF's value even after 100 ETTs. Better agreement is found in the case of the channels. Here the convergence at $y/h = 0.35$ is obtained after approximately 15 ETTs. However,
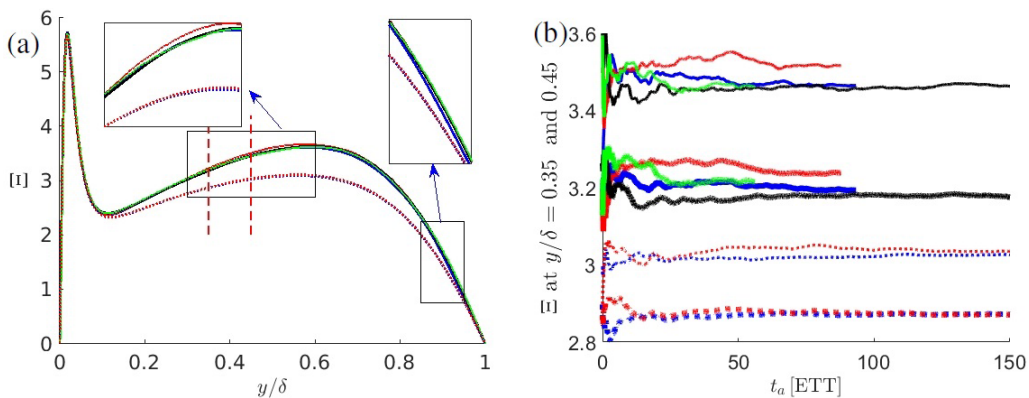

FIG. 3. (a) Indicator function Ξ for the six cases of Table I, depicting differences. (b) Values of Ξ at $y/\delta = 0.35$ and 0.45 as a function of averaging time t_a expressed in eddy-turnover times. Colors are as in Table I, with solid lines for pipes and dotted lines representing channels. Thick lines show $y/\delta = 0.35$ and thin lines $y/\delta = 0.45$.
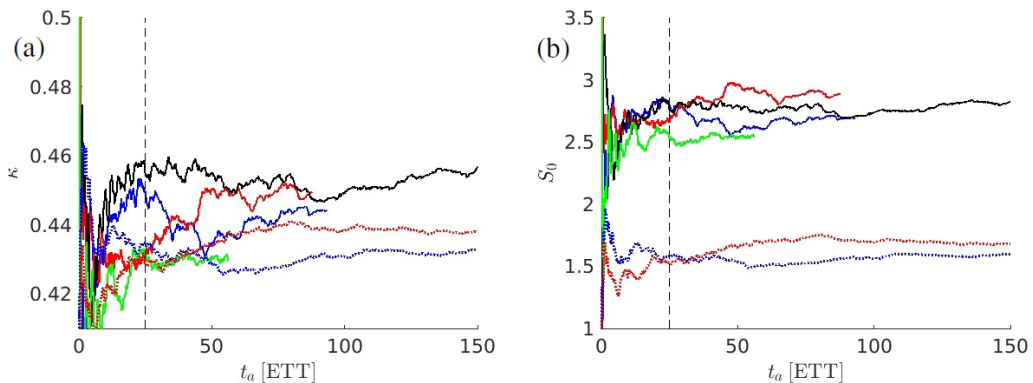
FIG. 4. Extracted overlap parameters (a) κ and (b) S_0 for the six cases of Table I as a function of averaging time t_a expressed in ETTs. Colors are as in Table I, with solid lines for pipes and dotted lines representing channels.

at $y/h = 0.45$ the differences are of the order of 2% after 80 ETTs, which is an extremely lengthy computation for high-Reynolds-number simulations.

The effect of this lack of adequate resolution can be better evaluated by the time-averaged values of the overlap coefficients κ, B, and S_0 as functions of ETT. After 50 ETTs, the differences among the cases are still above 3%, as shown in Fig. 4. Again, the convergence for the channel case is better, but there remains a small difference up to 150 ETTs, which corresponds to very expensive computations. In any case, at least 20 ETTs are needed to obtain some level of convergence. Such differences in the indicator function Ξ should be smaller for any reliable simulation to predict the values of the coefficients.

Finally, in the case of pipe flow, the values of these coefficients appear to depend on the azimuthal resolution, raising questions about the mesh aspect ratio of the grids. A careful study of such mesh-variation effects in flows near their singularities, as in the case around the axis of pipes, is highly recommended. Such a study should also examine the sensitivity of the indicator function Ξ to the order of the finite-difference scheme used in the DNS. In general, the results demonstrate that classical and commonly used mesh sizes in the wall-normal direction for DNSs are not sufficiently fine to extract coefficients of the overlap region in wall-bounded turbulent flows, such as κ and S_0, with good accuracy.

To further examine the sensitivities of DNS to various simulation parameters by accessible values of Re_τ while allowing a multitude of cases in a parametric study, we extended the cases of Table I to the $Re_\tau \approx 1000$ cases of Table II. In every case, the results of the turbulence intensities are below a difference of 1% for either normal or double resolution (not shown). In Fig. 5(a) we show Ξ for every case but the half-resolution cases. This is because they are absolutely wrong on the points close to the first minimum of Ξ, as seen in this figure's inset. The straight lines represent Eq. (4). As we can see, even if the curves collapse almost perfectly, the sensitivity is very large. This is shown in Fig. 5(b). Here κ and S_0 cannot be found with less than 3% difference among the best-resolved meshes and nearly converged cases we tested. Differences of as much as 8% are found between all the cases of Table II, including some with inadequate resolution (green cases) or different convergence or box sizes. For example, this creates a new uncertainty source in the estimation of the von Kármán coefficient that is very important for modeling and predicting wall-bounded turbulent flows, as highlighted recently by Monkewitz's careful evaluation [25].

To conclude, after carefully studying two different geometries with two trusted high-resolution codes, we have seen that evaluating derived quantities can be extremely difficult to obtain. In the case of the intensities and the mean streamwise velocity, the classical resolution seems to be enough to obtain errors below 0.5%. However, running these simulations for a very long time is
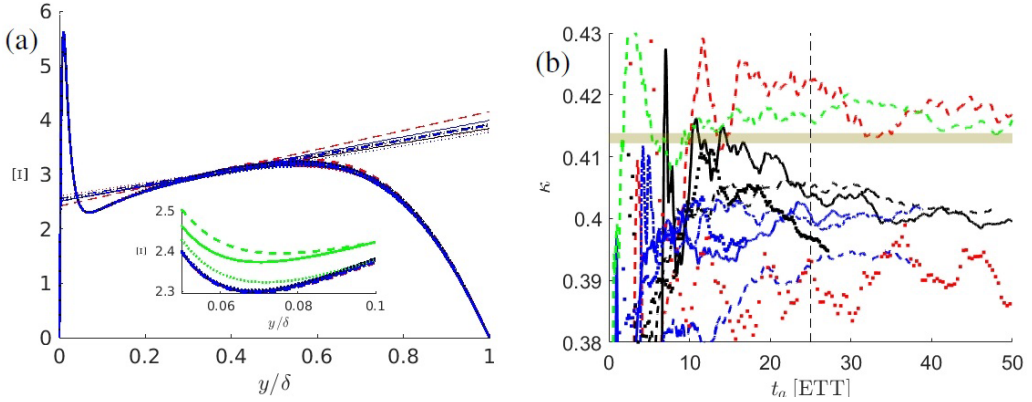
FIG. 5. (a) Indicator function Ξ for the cases of Table II, with straight lines depicting the log-lin overlap relation of Eq. (4) for each case and the inset depicting the limitations in cases with worst resolution by failing to capture the near-wall minimum value. (b) Range of extracted κ as a function of ETT for cases displayed with line types and colors shown in Table II, with the best-resolved cases for $Re_\tau \approx 1000$ yielding $\kappa \approx 0.4$ and $S_0 \approx 1.5$. The parameters extracted from Eq. (4) for converged higher $Re_\tau \approx 5200$ are shown by the wide yellow line: $\kappa \approx 0.413$ and $S_0 \approx 1.15$ [3,15].

necessary. Below 10 ETTs, the statistics exhibit a significant level of noise. The log-lin model of MN [11] compared to the pure logarithmic model has allowed evaluation of the sensitivities of their parameters, which are extremely high. Errors of around 3% on the computation of these parameters are expected for large Reynolds numbers. Moreover, running 50 ETTs for very large simulations is almost impossible.

The data used for this paper can be obtained by contacting the authors.

[1] S. Hoyas and J. Jiménez, Scaling of the velocity fluctuations in turbulent channels up to $Re_\tau = 2003$, Phys. Fluids **18**, 011702 (2006).

[2] M. P. Simens, J. Jimenez, S. Hoyas, and Y. Mizuno, A high-resolution code for turbulent boundary layers, J. Comput. Phys. **228**, 4218 (2009).

[3] M. Lee and R. Moser, Direct numerical simulation of turbulent channel flow up to $Re_\tau \approx 5200$, J. Fluid Mech. **774**, 395 (2015).

[4] S. Hoyas, M. Oberlack, F. Alcántara-Ávila, S. V. Kraheberger, and J. Laux, Wall turbulence at high friction Reynolds numbers, Phys. Rev. Fluids **7**, 014602 (2022).

[5] S. Hoyas and M. Oberlack, Turbulent Couette flow up to $Re_\tau = 2000$, J. Fluid Mech. **987**, R9 (2024).

[6] C. M. Millikan, in *Proceedings of the 5th International Congress on Applied Mechanics* (Wiley, New York, 1938).

[7] R. Vinuesa, P. Schlatter, and H. M. Nagib, Role of data uncertainties in identifying the logarithmic region of turbulent boundary layers, Exp. Fluids **55**, 1751 (2014).

[8] H. M. Nagib and K. A. Chauhan, Variations of von Kármán coefficient in canonical flows, Phys. Fluids **20**, 101518 (2008).

[9] M. Oberlack, S. Hoyas, S. V. Kraheberger, F. Alcántara-Ávila, and J. Laux, Turbulence statistics of arbitrary moments of wall-bounded shear flows: A symmetry approach, Phys. Rev. Lett. **128**, 024502 (2022).

[10] F. Alcántara-Ávila, L. M. García-Raffi, S. Hoyas, and M. Oberlack, Validation of symmetry-induced high moment velocity and temperature scaling laws in a turbulent channel flow, Phys. Rev. E **109**, 025104 (2024).

[11] P. Monkewitz and H. Nagib, The hunt for the Kármán 'constant' revisited, J. Fluid Mech. **967**, A15 (2023).

[12] N. Afzal and K. Yajnik, Analysis of turbulent pipe and channel flows at moderately large Reynolds number, J. Fluid Mech. **61**, 23 (1973).

[13] J. Jiménez and R. D. Moser, What are we learning from simulating wall turbulence? Philos. Trans. R. Soc. A **365**, 715 (2007).

[14] V. Baxerres, R. Vinuesa, and H. Nagib, Evidence of quasiequilibrium in pressure-gradient turbulent boundary layers, J. Fluid Mech. **987**, R8 (2024).

[15] H. Nagib, R. Vinuesa, and S. Hoyas, Utilizing indicator functions with computational data to confirm nature of overlap in normal turbulent stresses: Logarithmic or quarter-power, Phys. Fluids **36**, 075145 (2024).

[16] J. Schumacher, K. R. Sreenivasan, and V. Yakhot, Asymptotic exponents from low-Reynolds-number flows, New J. Phys. **9**, 89 (2007).

[17] R. Vinuesa, C. Prus, P. Schlatter, and H. Nagib, Convergence of numerical simulations of turbulent wall-bounded flows and mean cross-flow structure of rectangular ducts, Meccanica **51**, 3025 (2016).

[18] A. Lozano-Durán and J. Jiménez, Effect of the computational domain on direct simulations of turbulent channels up to $Re_\tau = 4200$, Phys. Fluids **26**, 011702 (2014).

[19] F. Lluesma-Rodríguez, S. Hoyas, and M. Peréz-Quiles, Influence of the computational domain on DNS of turbulent heat transfer up to $Re_\tau = 2000$ for $Pr = 0.71$, Int. J. Heat Mass Transf. **122**, 983 (2018).

[20] J. Yao, S. Rezaeiravesh, P. Schlatter, and F. Hussain, Direct numerical simulations of turbulent pipe flow up to $Re_\tau \approx 5200$, J. Fluid Mech. **956**, A18 (2023).

[21] F. Alcántara-Ávila, S. Hoyas, and M. Pérez-Quiles, Direct numerical simulation of thermal channel flow for $Re_\tau = 5000$ and $Pr = 0.71$, J. Fluid Mech. **916**, A29 (2021).

[22] F. Lluesma-Rodríguez, F. Álcantara-Ávila, M. Pérez-Quiles, and S. Hoyas, A code for simulating heat transfer in turbulent channel flow, Mathematics **9**, 756 (2021).

[23] L. Yu, M. Z. Yousif, M. Zhang, S. Hoyas, R. Vinuesa, and H.-C. Lim, Three-dimensional ESRGAN for super-resolution reconstruction of turbulent flows with tricubic interpolation-based transfer learning, Phys. Fluids **34**, 125126 (2022).

[24] J. Jiménez and S. Hoyas, Turbulent fluctuations above the buffer layer of wall-bounded flows, J. Fluid Mech. **611**, 215 (2008).

[25] P. A. Monkewitz, On the difficulty of determining Kármán "constants" from direct numerical simulations, Phys. Fluids **36**, 045162 (2024).